Stealth mRNA nanovaccines to control lymph node trafficking

Coral García-Fernández [a,b], Tommaso Virgilio [b], Irene Latino [b], Marta Guerra-Rebollo [a], Santiago F. Gonzalez [b], Salvador Borrós [a], Cristina Fornaguera [a,*]

[a] Grup d'Enginyeria de Materials (Gemat), Institut Químic de Sarrià (IQS), Universitat Ramon Llull (URL). Via Augusta, Barcelona, Catalonia, 08017, Spain
[b] Institute for Research in Biomedicine, Faculty of Biomedical Sciences, Universita della Svizzera italiana (USI) – Switzerland, Via Francesco Chiesa 5, Bellinzona 6500, Suiza

ABSTRACT

mRNA-based vaccines symbolize a new paradigm shift in personalized medicine for the treatment of infectious and non-infectious diseases. However, the reactogenicity associated with the currently approved formulations limits their applicability in autoinflammatory disorders, such as tumour therapeutics. In this study, we present a delivery system showing controlled immunogenicity and minimal non-specific inflammation, allowing for selective delivery of mRNA to antigen presenting cells (APCs) within the medullary region of the lymph nodes. Our platform offers precise control over the trafficking of nanoparticles within the lymph nodes by optimizing stealth and targeting properties, as well as the subsequent opsonization process. By targeting specific cells, we observed a potent adaptive and humoral immune response, which holds promise for preventive and therapeutic anti-tumoral vaccines. Through spatial programming of nanoparticle distribution, we can promote robust immunization, thus improving and expanding the utilization of mRNA vaccines. This innovative approach signifies a remarkable step forward in the field of targeted nanomedicine.

1. Introduction

An elegant "magic bullet" approach was the inspiration behind nanomedicine over a century ago [1]. Today, the application of nano-technology in medicine still holds the promise of delivering active components to target specific cell populations, while reducing off-target effects and improving prophylactic and therapeutic efficacy [1–3]. In particular, recent advances in our understanding of immunomodulation and mRNA technologies underpin the urgency of developing target delivery strategies to transfer this knowledge into effective nano-based vaccines [4,5]. To this end, lessons learnt from the recognition of immune complexes and particulate antigens by the immune system emphasize the relevance of the lymph nodes (LNs), as the epicentre location of the immune response [6]. LNs-resident Antigen Presenting Cells (APCs), such as dendritic cells (DCs) and macrophages, are specifically engaged to activate the adaptive immune system against a variety of infectious and non-infectious diseases, such as cancer [7,8]. Moreover, the antigen response occurring in the LNs is pivotal for antibody production. This extensive knowledge on the immunological mechanisms occurring after antigen recognition can benefit the design of next-generation nanovaccines. By controlling the trafficking of the

nanoparticles in these secondary lymphoid organs, selective modulation of APCs can be achieved, eliciting potent immunization.

The architecture of the LNs is designed to orchestrate an efficient reaction after vaccine administration and lymphatic drainage [9,10]. LNs are bean-shaped organs, surrounded by a collagenous capsule. They present multiple afferent lymphatics opening to the subcapsular sinus (SS) region, where the homonymous subcapsular sinus macrophages (SSMs) reside. These leukocytes are interspersed within the lymphatic endothelial cells (LEC) structuring the cortex of the subcapsular sinus. Both SSMs and LECs constitute the sorting architecture for the different complexes and bodies arriving to the LNs, including nanoparticles. Following arrival to the LNs via afferent vessels, different trafficking routes for nanoparticles have been documented depending on their size [11,12]. On the one hand, small particles (<50 nm) are reported to cross the SS along the interstitial gaps between SSMs and LECs. Rapid access to the underlying B follicles and T cell areas can also be reached by conduit-mediated transfer or transcytosis. On the other hand, larger particles (>100 nm) are usually engulfed by SSMs, which can then transfer them to B cells. These trafficking routes demonstrate that the size of nanoparticles determines their access to the medulla of LNs. However, existing nanovaccines (larger than 100 nm) face challenges in

---

* Corresponding author.
  E-mail address: cristina.fornaguera@iqs.url.edu (C. Fornaguera).

reaching medullary dendritic cells and macrophages (MMs), limiting their ability to induce specific T-cell activation and ensure long-term antibody responses.

Interestingly, recent discoveries describe size as a determinant factor for nanoparticle distribution in the LNs, pointing out complement protein opsonization as the underlying mechanism [13–15]. *Zhang* et al. [12] demonstrated that greater particle diameter enhance C3 opsonization of the nanomedicines, which is consistent with the relatively large size of C3b protein. Small particles lack sufficient area to adsorb C3b molecules and consequently they do not attach to the surface of nanoparticles. Thus, C3 complement adsorption on larger nanoparticles is responsible for their binding to SSMs and their further shuttle and exposure to cognate B cells in the LNs, preventing nanoparticle to target DCs and MMs in the medulla. It is therefore necessary to design stealth (bio)materials to efficiently reach the medullary region of the LNs, and selectively target APCs to modulate both humoral and cellular immune response [12].

As a result of the opsonization-regulated transport of nanoparticles in the LNs, the long-standing paradigm of protein corona in nanomedicines emerges once again as a barrier to control their biological identity. Several approaches have been developed during the last decade to achieve stealth properties for controlled spatial release after systemic administration and blood exposures, although these strategies have been less developed for lymphatic delivery [16,17]. Among them, poly (ethylene glycol) (PEG) engineered nanosystems are the gold standard method for targeting nanoformulations while reducing opsonization and rapid clearance. However, concerns have arisen following the massive vaccination against SARS-CoV-2 [18–20]. The widespread rollout of pegylated mRNA-based COVID-19 nanovaccines highlighted the modest anti-fouling performance and the poor understanding of PEG immunogenicity, compromising booster vaccination doses and their administration for autoimmune and autoinflammatory diseases [21–25]. Moreover, current lipidic formulations demonstrate high reactogenicity, evidencing the necessity of optimize nanovaccines to improve immunogenicity without enhancing reactogenicity. With these factors, as well as the potential benefits of APC-targeted vaccines, the development of balanced stealth-targeted materials could greatly improve novel and safe immunization strategies [26].

Thus, the next generation of nano-based vaccines showing improved cell targeting properties, together with the adaptability of mRNA technology, can change the game of immunization tools. To address the size-restricted nature of LN NPs trafficking, we developed new stealth materials for nanoparticle formulation that are easy to customize for targeted delivery. Herein, we present a novel family of antifouling graft polymers for mRNA vaccination applications. In particular, these polymers exhibit a backbone of cationic oligopeptide-end. Modified poly (beta amino esters) (OM-pBAE) [27]. Additionally, the side chains were chemically modified for the first time to copolymerize zwitterionic monomers, which have a strong ability to bind water molecules, preventing protein corona formation on the surface of nanoparticles [28–31]. The resulting graft polymer, named ZION (ZwitterIONic), allows polyplex assembly, showing significant advantages for preventing protein adsorption. Firstly, the cationic block allows complexing negatively charged mRNA molecules and enables endosomal escape of the NPs after cellular uptake, as described in our earlier research [27,32,33]. Secondly, the zwitterionic graft provides antifouling properties to the polymer, as we have previously demonstrated for other applications [34,35]. Thirdly, ZION can be vectorized against LN resident APCs by using polymer peptide-functionalization to target CLEC9A receptor present in these populations [36–38]. Finally, characterization of the pharmacodynamic and kinetic profile of ZION particles and further evaluation of their capacity to specifically boost antigen presentation *in vivo*, in a tumour vaccine model, demonstrate the target potential of this new delivery system.

Therefore, the current work provides new insight into the formulation of stealth-targeted nanoparticles for prophylactic and therapeutic anti-tumoral mRNA vaccination purposes. By minimizing the direct inflammation response arose by current lipidic formulations [39], the described ZION formulation allows to extend mRNA technology to the treatment of autoinflammatory disorders, including cancer. We demonstrated *in vivo* that this novel nanoplatform efficiently targets LN residing APCs and elicits a potent cellular and humoral anti-tumoral response.

2. Results and discussion

2.1. RAFT-mediated grafting of sulfobetaine provides stealth properties

ZION polymers were synthesized using the 'grafting from' method, through reversible addition fragmentation chain transfer (RAFT) living polymerization [34] of methacrylate sulfobetaine monomers on the side chains of the poly (β-aminoester) (pBAE) backbone (Supplementary method 1–3, Supplementary Fig. 1). The average length of the grafted zwitterionic chains was determined to be ~15 monomers (approximately 25% of the total side chains modified) (Supplementary Fig. 2). Further modification of the lysine oligopeptide on the acrylate ends of the original pBAE was performed *via* the Michael addition reaction to improve the interaction of the nanoparticles with the cell membrane, as described in our previous work [27]. The ZION polymers obtained were mixed with histidine modified-pBAE (H-pBAE) and mRNA at different weight ratios in sodium acetate buffer (*w*/w, pH 5.2) (Method 1 and 2, Supplementary Fig. 3). Following our previous results [27,40], H-pBAE was also included in the formulation to enhance the effect of the proton sponge and promote endosomal scape after cell uptake (Fig. 1a). The presence of both ZION and H-pBAE polymers and their proximity to the nucleic acid in the nanoparticles was confirmed by FRET measurements (Supplementary Fig. 4), following *Navalón* et al. [41] method. The ZION nanoparticles (ZION NPs) showed slightly polydisperse populations with hydrodynamic sizes in the range of 190–210 nm and ζ-potential at around +20 mV (Fig. 1b and 1c). Additionally, these results were confirmed by transmission electronic microscopy (TEM), (Fig. 1d and 1e). As the control sample, non-grafted histidine and lysine oligopeptide modified pBAE (OM-pBAE) nanoparticles were prepared on mixing with mRNA and the obtained OM-pBAE particles showed size and surface charges comparable to those of ZION NPs. Moreover, we optimized and reported the stability of the formulations up to 4 months after lyophilization and long-term storage at −20 °C, which is a convenient storage temperature for logistics and supply chains (Supplementary Fig. 5).

Incubation of the formulated NPs in PBS dilution of human serum confirmed the antifouling performance of the zwitterionic grafting on ZION NPs. Direct consequences of the reduced protein corona were evidenced by examination of the NPs in serum-containing and serum-free media conditions with transmission electron microscopy (Fig. 1f). The fact that exposure to protein-rich media does not induce aggregation or shape distortion of ZION NPs in comparison to traditional OM-pBAE NPs, shows that the presence of the zwitterionic side chains improves the colloidal stability under these conditions. Total quantification of the adsorbed proteins on the surface of the NPs after different incubation times in human sera-diluted media verified the predictable reduction of attached proteins on ZION NPs (Fig. 1 g).

2.2. The addition of a targeting peptide balances the targeting and stealth properties

To explore the possible combination of the zwitterionic stealth properties with target delivery, we investigated the addition of a targeting peptide in the ZION NPs formulation (Fig. 2a). The WH peptide is an 11 amino acid length peptide previously described for its specificity for the CLEC9A receptor, a C-type lectin receptor restricted mainly to type I conventional dendritic cells (cDC1) and MMs in humans [36]. This type I membrane protein recognizes and internalizes F-actin, a cytosolic protein exposed when the cell membrane is damaged. The underlying
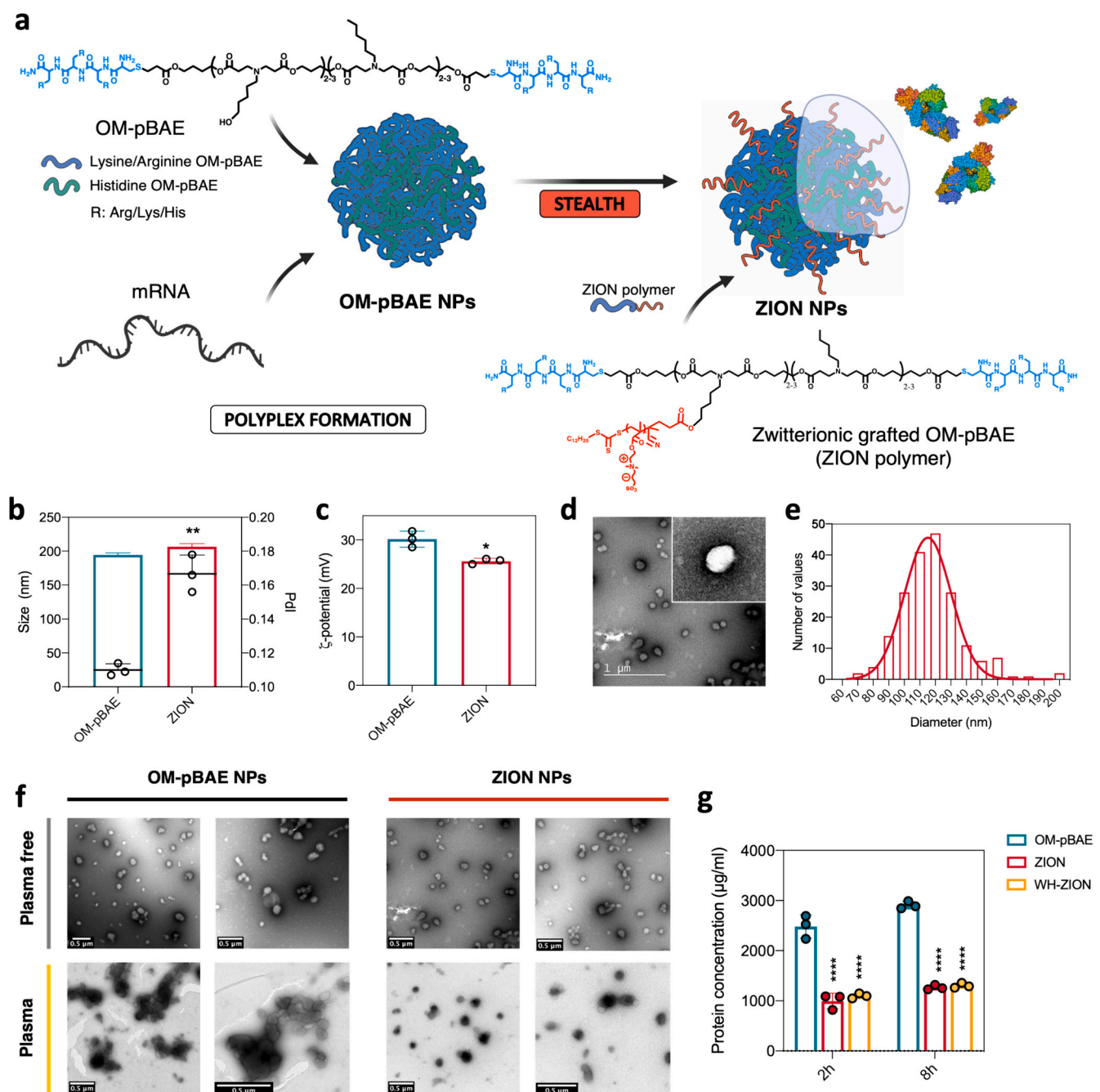
Fig. 1. mRNA polyplexes preparation and characterization. Schematic representation of **a)** OM-pBAE (left) and ZION NPs (right) preparation by mRNA complexation. Anti-fouling properties of the stealth polyplexes. **b)** Hydrodynamic diameter and polydispersity index. (PdI), by Dynamic Light Scattering (DLS) of the OM-pBAE and ZION NPs. (mean±standard deviation). $n = 3$ and 10 subruns per measurement. The average size is 194 nm for OM-pBAE NPs and 206 nm for ZION-NPs. Polydispersity index is <0.2 for both candidates. (* $p < 0.05$ and ** $p < 0.01$, *t*-test). **c)** ζ-potential measurement, by. DLS, of the OM-pBAE and ZION NPs. $n = 3$ and 10 subruns per measurement. (mean±standard deviation). The average ζ-potential is +30 mV for OM-pBAE NPs and + 25 mV in ZION NPs. (* $p < 0.05$ and ** $p < 0.01$, *t*-test). **d)** Representative transmission electron microscopy (TEM) image of NPs. Scale bar 1 μm. Representative of $n = 2$ independent experiments. **e)** Histogram distribution of the ZION NPs' diameter (bin = 10) obtained by ImageJ image analysis software. Later, Prism 8 software was used to obtain the Gaussian curve fitting for histogram model. $n > 150$. **f)** Representative transmission electron microscopy (TEM) micrographs of OM-pBAE and ZION NPs with and without (in preparation buffer) human serum dilution incubation. Samples were prepared as described in the methods and then incubated in 1:10, *v*/*v* dilution of human serum in phosphate buffer solution (PBS, pH 7) for 2 h. Images were acquired without washing nor centrifugation steps. Scale bar = 0.5 μm. **g)** Quantification of the total protein adsorbed on the surfaced of OM-pBAE, ZION and WH-ZION NPs after 2 and 8 h incubation in human serum dilution in PBS (pH 7, 1:10, *v*/*v*). Proteins were isolated by centrifugation and denaturalized with SDS agent. Quantification by Bicinchoninic acid colorimetric assay is represented as the mean±standard deviation. $n = 3$. For the multiple comparison, *P* value was calculated by one-way ANOVA with Tukey *post hoc* test without any adjustment. **** $p < 0.0001$.

interest in this target is not only in the ability of cDC1s to engage cross-presentation, which induces T cell activation and high antibody production without adjuvants, but also in the direct interaction of MMs with cDC1s for antigen presentation [38,42,43].

The WH targeting peptide was introduced into the H-pBAE fraction of the ZION NPs. This polymer is highly modifiable because of the presence of the hydroxyl group in the side chains of the backbone, creating multiple modifiable points for derivatization. To assay the
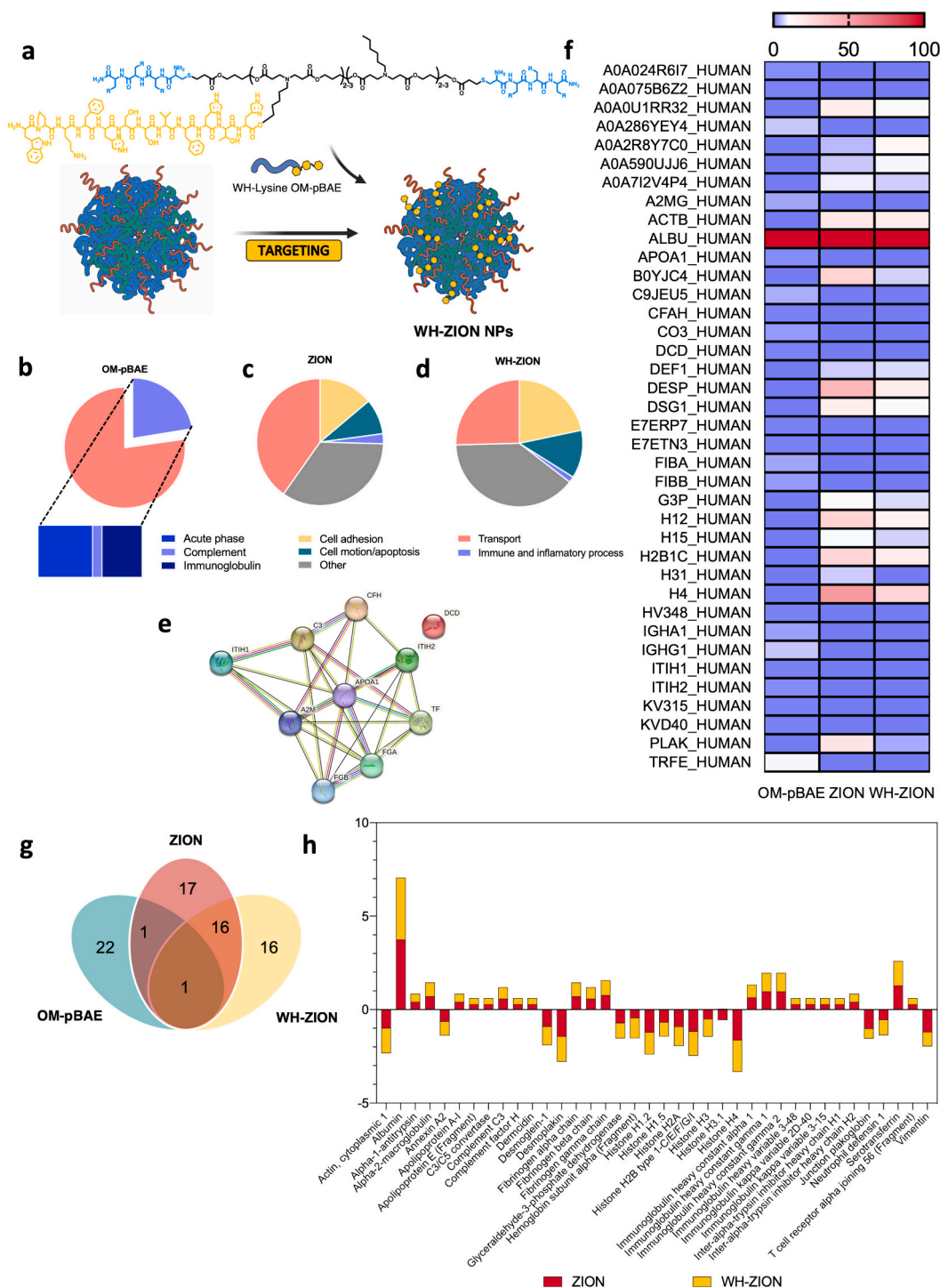
Fig. 2. Protein corona characterization and WH peptide modification of ZION NPs. a) Schematic representation of the WH peptide modification of the ZION NPs to formulate targeted WH-ZION NPs. **b-d)** Classification and relative contribution of identified corona proteins in **b)** OM-pBAE, **c)** ZION and **d)** WH-ZION NPs by LC/MS. Proteins were classified in five groups and particularly immune related proteins in OM-pBAE NPs were further divided in three subcategories depending on their role in the immune response. **e)** Protein-protein interaction network of the identified complement system related proteins (described in Fig. 2f). STRING online database was used to elaborate the scheme. **f)** Normalized (to the most abundant) percentage of each corona protein from human serum represented as a heatmap. Blue shows absence and red, abundance of the protein. See Supplementary table S2 to identify the corona proteins representing each row of the heatmap (UniProtKB database code). *n* = 2. **g)** Venn diagram demonstrating the shared proteins identified on the surface of the OM-pBAE, ZION and WH-ZION NPs. **h)** Relative abundance (z score) of each corona protein sample compared to OM-pBAE NPs corona. Z score among samples was calculated following Voge et al. methodology [46]. (For interpretation of the references to colour in this figure legend, the reader is referred to the web version of this article.)

optimal percentage of targeting peptides in the ZION formulation, different ratios were introduced into the formulation and specificity was tested *in vitro* (Supplementary Fig. 6). The fact that the maximum ratio of the target peptide is not translated in the highest percentage of transfections may indicate the saturation of the cellular receptors or a decrease in the bioavailability of the peptide to interact with CLEC9A [44].

In addition to dramatically reducing the adsorption of proteins on the surface of the nanoparticles, integrated zwitterionic grafting is hypothesized to prevent complement system cascade activation and their further opsonization of the particles. Preliminary SDS-PAGE analysis revealed the prevalence of a protein band observed in MW between 60 and 80 kDa, most likely albumin, independently of the formulation. However, a change in protein patterns was detected for ZION NPs, with an increase of low molecular weight proteins in the corona (Supplementary Fig. 7). LC/MS analysis of the proteins isolated from the protein corona of the NPs confirmed the absence of complement factor proteins and the enrichment of small intrinsic disordered proteins on the surface of ZION and WH-ZION NPs (Fig. 2c and d). In contrast, complement factors and immunoglobulins were found on the surface of OM-pBAE NPs, confirming the stealth activity of the zwitterionics. >20% of the proteins detected on OM-pBAE NPs were involved in the inflammation and opsonization processes (Fig. 2b). The notable presence of complement C3, factor H and convertase C3/C5 suggests alternative activation of the complement system [45] (Fig. 2e). NPs were used in cytotoxicity and haemolysis assays to exclude the influence of NPs on cellular lysis as the cause of enrichment of intracellular proteins in the ZION and WH-ZION NPs corona (Supplementary Fig. 8 and 9). Overall, proteins from the extracellular matrix and small hydrophilic proteins were detected in the protein fraction of ZION and WH-ZION NPs, suggesting the importance of the hydrophobic forces over electrostatic interactions driving the protein corona formation in these particles (Fig. 2f). The resulting pattern of adsorbed proteins on the surface of ZION and WH-ZION NPs were nearly identical, demonstrating the strong stealth effect of the polysulfobetaine in the formulation (Fig. 2g and h).

2.3. NPs trafficking routes in the LN are complement-dependent

To evaluate lymphatic drainage and selective accumulation in the lymph nodes (LNs), luciferase mRNA polyplexes were administered *via* two routes in mice: intramuscularly (IM) into the hindlimb skeletal muscle and subcutaneously (SC) into the footpad. Upon administering the original OM-pBAE NPs, no signal was detected through either route, indicating the rapid clearance of the NPs. To conduct further analysis and compare the candidates, the OM-pBAE NPs were reformulated by incorporating PEG as a stabilizer, resulting in OM-pBAE-PEG NPs, following our previously explored methodology in *Brugada* et al. [47] This formulation aimed to decrease clearance time and enhance the effectiveness of the NPs after administration.

Subcutaneous administration of OM-pBAE-PEG NPs resulted in their accumulation in the lymph nodes (LNs), whereas IM administration only showed a noticeable signal at the injection site, suggesting a lack of lymphatic drainage following this route (refer to Supplementary Fig. 10 and Fig. 11). In contrast, both SC and IM administration of WH-ZION NPs led to rapid accumulation in the popliteal LNs (pLNs). The reduced signal observed following the administration of ZION NPs can be attributed to two factors: nonspecific transfection and the ability to evade rapid clearance (Supplementary Fig. 11). Consequently, the results obtained from BLI imaging underscore the importance of zwitterionic grafting in preventing rapid clearance after administration, as well as the specific targeting achieved through the combination of the WH peptide and stealth grafting.

To compare the sub-organ the preferred accumulation region within the LN for the different candidates, we collected the popliteal LNs (pLNs) at 2 h post footpad injection for imaging characterization. According to the anatomical and microstructural organization of the LNs described,

tightly packed conduits do not allow the diffusion of any of the candidates due to their large hydrodynamic size (∼200 nm). However, confocal images showed clear differences between candidates in their intralymph node transport (Fig. 3a). OM-pBAE-PEG nanoparticles appear to accumulate in the subcapsular sinus, where SSMs reside, apart from the medulla. This accumulation has been previously reported for C3 opsonized particulate antigens [48,49]. Typically, SSMs bind to C3 adsorbed NPs and shuttle them to the underlying B cells, which are ultimately responsible for their transport to follicular dendritic cells (FDCs). Particle uptake by SSM located in the SS is clearly observed upon injection of OM-pBAE-PEG NPs. On the contrary, stealth WH-ZION NPs were retained principally in the medullary region of the LN, where CLEC9A expressing dendritic cells (DC) and medullary macrophages (MM) reside. No SSM shuttling was observed for these nanoparticles. Qualitative two-photon microscopy imaging (Fig. 3b) and semiquantitative analysis (Fig. 3c) 24 h after SC administration showed homogenous accumulation of OM-pBAE-PEG NPs in the subcapsular sinus and medullary region of the LN, while WH-ZION NPs remained preferentially in the medulla.

The uptake and protein expression of GFP-mRNA NPs by different cell populations in the pLNs, including SSMs, MMs, DCs, and B cells at different timepoints were analysed using flow cytometry, which confirmed the imaging results (Fig. 3d) [50]. Administration of OM-pBAE-PEG NPs resulted in a remarkable accumulation in the SSMs at early timepoints, along with a noticeable signal in the B cell population. According to the presence of C3 complement on the surface of these NPs, these are expected to interact with SSMs through CR3 (Mac-1)/FcRIIb receptors and, subsequently, be shuttled to the underlying B cells, where they interact through CD21 and CD35 complement receptors (Fig. 3e). Additionally, the fact that the GFP reporter mRNA was not expressed despite their high uptake by SSMs can be attributed to the ability of FcRIIb to recycle antigens to the surface without entering the lysosomal compartment [51] (Supplementary Fig. 12). Regarding the medullary cell populations, a high accumulation was also observed up to 6 h after administration, likely due to the saturation of the cortex with the abundant presence of NPs at early time points. Interestingly, WH-ZION NPs did not show binding to SSMs or B cells, confirming the stealth properties of vehicles and the hypothesized role of C3 in the trafficking of NPs (Fig. 3e). Administration of these NPs also resulted in substantial targeting of MMs and DCs in the medulla. The sustained accumulation of WH-ZION NPs up to 48 h after injection suggests the specificity of the targeting and the arrival of DCs transfected at the site of injection *via* the lymphatics. NP uptake by CD11b⁻ DC, neutrophils, natural killer and T cells was also evaluated but found to be negligible except for OM-pBAE-PEG in neutrophils (Supplementary Fig. 13). This can be attributed, as previously stated, to complement-driven phagocytosis reported in this population of cells. Finally, analysis of ZION served as a control, demonstrating limited interaction with resident lymph node cells.

2.4. Targeted mRNA delivery elicits effective, adaptive and specific immune response

The general characterization of the biodistribution of NPs in the LNs confirmed the critical role of opsonization in the specific uptake of NPs by the phagocytic compartment. The efficacy of NPs as possible vaccine platforms was then evaluated by assessing the prescribed systemic proinflammatory response and the humoral and cellular immune response. We set out to study the secretion of cytokines related to systemic inflammatory mechanisms *in vivo* by formulating the NPs complexing ovalbumin (OVA) mRNA. The increase in cytokine release measured after OM-pBAE-PEG NPs administration was significantly higher than the concentrations detected for ZION and WH-ZION NPs (Fig. 4a). In addition, targeting CLEC9A for DCs vaccination strategies induces tolerance, which increases the interest of this approach as a dual role limiting inflammation and targeting in immuno-based therapies [50]. Consistently with previous results, IL-6 is produced upon administration
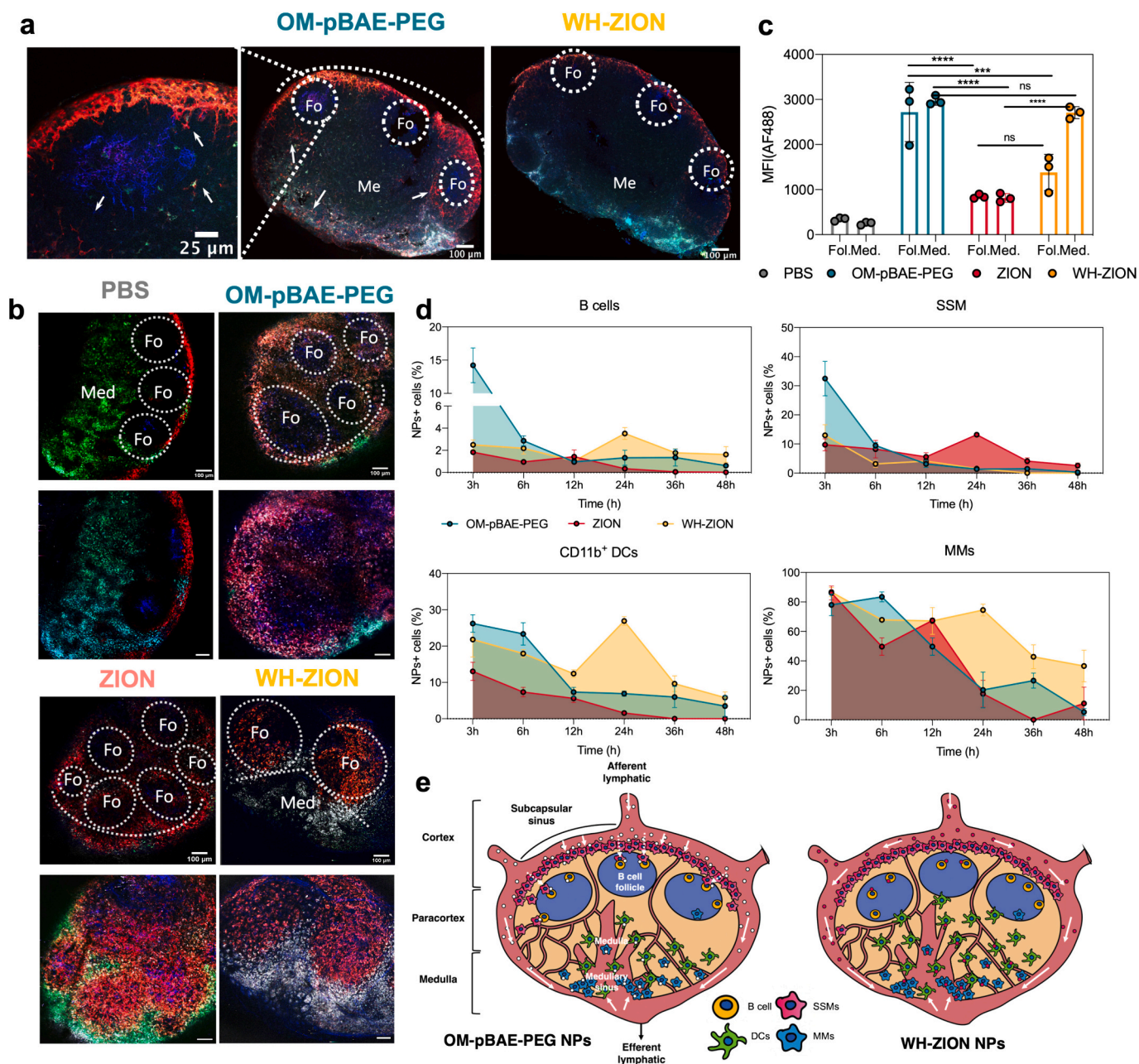
Fig. 3. Preferential accumulation of the different nanoparticles in the popliteal LNs regions. a) Confocal image of a section showing the representative cell populations of the LN based on the expression of the markers of macrophages (CD169+, red), follicular dendritic cells (CD21/35+, blue) and dendritic cells (CD11c+, green). NPs are shown in white. NPs were injected in the footpad of C57BL mice (10 µL) and collected 6 h later. *n* = 3. Magnification of OM-pBAE-PEG NPs represents the nanoparticle shuttle by SSMs (arrows) to the subcapsular sinus underlying cognate B cells. Scale bar = 100 µm. **b)** Two-photon imaging showing representative cell populations of the LN based on the expression of the markers of macrophages (CD169+, red), follicular dendritic cells (CD21/35+, blue) and dendritic cells (CD11c+, green). NPs are shown in white. NPs were injected in the footpad of C57BL mice (10 µL) and collected 6 h later. n = 3. Lower images show a maximum intensity projection of the whole z-stack of the LN, while upper row images show a slice with the different regions highlighted (Fo = follicles, M = medulla). **c)** Quantification of the total MFI related to each labelled NPs in the medullary and follicular region of the LNs. Images were quantified using ImageJ software. Two-way ANOVA, Turkeys multiple comparison test. To simplify the interpretation, the comparisons were made only between groups of injected NPs and the same region of the LN. The differences considered significant for *$p < 0.05$; **$p < 0.01$; ***$p < 0.001$; ****$p < 0.0001$. Results are expressed as mean±standard deviation. **d)** NPs were injected in the footpad of C57BL mice (10 µL) at different timepoints and collected at the end of the experiment, enzymatically digested and analysed by flow cytometry. Cellular uptake of NPs by B cells, SSMs, DCs and MMs is shown (see Supplementary Fig, 13 for the rest of populations mentioned in the text). Three LNs were analysed per condition. Results are expressed as mean±standard deviation. **e)** Schematic representation of the anatomical position of the major phagocytic populations in the LN and circulation pathway of opsonised OM-pBAE-PEG NPs (left) and stealth WH-ZION (right). SSMs are located in the subcapsular sinus area in close proximity to the B cell follicles (Fo), while MMs are mainly located in the medulla. White arrows represent the circulation of the nanoparticles-loaded lymph. (For interpretation of the references to colour in this figure legend, the reader is referred to the web version of this article.)
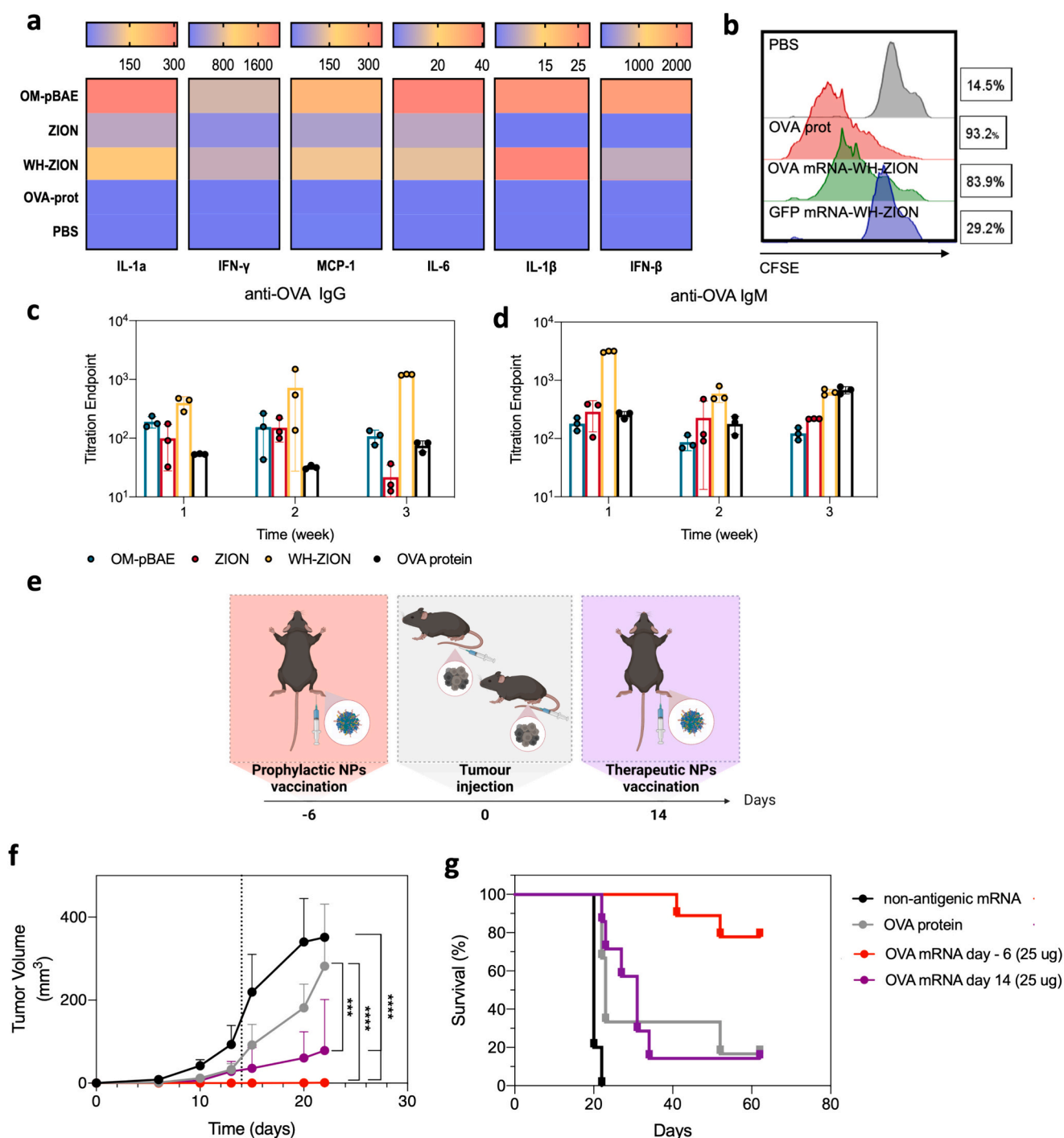
Fig. 4. Characterization of the inflammatory and adaptive response, and tumour growth inhibition elicited by WH-ZION NPs. a) Panel of inflammatory cytokines detected in the serum of mice. Mice were SC vaccinated with the NPs 7 days before collecting the sera. Legend show the concentration of each cytokine in pg/mL. $n = 3$. b) *Ex vivo* OVA specific $CD8^+$ T cell proliferation assay. OVA specific $CD8^+$ T cells were isolated from OTI/RAG mice and labelled with CFSE for further proliferation tracking. DCs were isolated from splenocytes of C57BL mice and enriched by using $CD11c^+$ microbeads. DCs were primed for 4 h with the NPs and then, co-cultured with $CD8^+$ T cells for 3 days. $n = 3$. c,d) ELISA titration assay over 3 weeks after vaccination. Briefly, mice ($n = 3$/group) were SC administered with the indicated formulation. Then, mice sera at 1, 2 or 3 weeks post vaccination were measured by ELISA to determine the endpoint titration of OVA specific IgG (4c) and IgM (4d) antibodies. e) Vaccination scheme for the prophylactic and therapeutic approaches. f) Tumour growth inhibition study of B16F1 melanoma. g) Kaplan-Meier survival curves of tumour-bearing mice are shown. Statistical significance was calculated by Student's t-test ***$p < 0.001$; ****$p < 0.0001$.

of OM-pBAE-PEG NPs, as a result of the interaction of these NPs with the underlying subcapsular sinus B cells. We also suggest that the high uptake of OM-pBAE-PEG NP by macrophages and neutrophils in pLNs is the main factor contributing to the pro-inflammatory response of IL-1 and MCP-1. The secretion of IL-1, the initiator of an innate immune cascade with potential adverse effects, is related to high reactogenicity

and immunogenicity [52]. Although this pro-inflammatory response can act as an adjuvant effect for the vaccine, it is not desirable for administration in patients with autoimmune or autoinflammatory diseases [53].

Reducing the inflammatory systemic response is typically associated with a limited adaptative response of the vaccine [54]. To recapitulate

this paradigm, we hypothesized the interplay of efficient target delivery and reduced inflammation to achieve a successful vaccine immunization performance. The ability of the different NPs to elicit an effective humoral response was verified by titration of the antibodies produced after vaccination over 3 weeks (Fig. 4 c and d). Plasma IgG and IgM anti-OVA binding titers were measured by enzyme-linked immunosorbent assay (ELISA). OM-pBAE NP administration demonstrated lower antibody secretion, suggesting a less efficient response than that of WH-ZION NPs. The latter induced a strong initial secretion of IgM, the first antibody secreted during the adaptive immune response, complementary to a time-increasing secretion of IgG. Unlike IgM, IgG antibodies are highly antigen specific, and their presence is typically associated with long-term immune protection [50].

The fact that WH-ZION NP vaccination induced higher levels of antibodies than OM-pBAE-PEG NPs without directly reaching the follicles upon arrival of the LN suggested stimulation of B cells through possible activation of APCs and T cell priming. In addition, the main focus of cancer vaccination strategies is the induction of robust cytotoxic CD8$^+$ T cell responses activated by DC cross-presentation. To test the capacity of NPs to prime and activate CD8$^+$ T cells, we conducted an *ex vivo* proliferation assay of OTI CD8$^+$ T cells isolated from naïve OTI/RAG mice. Cell proliferation induced by WH-ZION NPs, tracked by the CFSE signal, was comparable to that elicited by DC priming with OVA protein alone (Fig. 4b). Although there is no direct correlation between mRNA and protein administration, incubation of 1 μg of OVA mRNA WH-ZION NPs elicited a significant immune response in terms of CD8$^+$ T cell proliferation, likely related to the role of CLEC9A receptor pathways in the cross-presentation process [43].

2.5. WH-ZION NPs inhibit tumour growth and metastasis

We finally sought to determine whether the targeted WH-ZION NPs can be used as an anti-tumour platform for prophylactic vaccination in an OVA melanoma model (Fig. 4e-g). Prophylactic SC administration of WH-ZION NP resulted in the absence of tumour development during the whole experimental time (up to 20 days) after injection of melanoma B16F1/OVA cells, while vaccination with the OVA protein (positive control) led to a modest delay in tumour growth observable starting from 10 days after tumour injection. Additionally, the WH-ZION NP prophylactic vaccinated group exhibited a higher survival rate (78%) compared to OVA protein administration (17%). Apart from the inhibition of tumour growth, the metastatic capacity was performed on the sentinel LN that drains from the footpad by semiquantitative evaluation of the lymphoid organs. OVA B16F1 cells are easily recognized due to high melanin production, allowing the collected LNs to be classified as metastatic (value = 1) and non-metastatic (value = 0) and stablishing a binary value table. The results showed that prophylactic administration of WH-ZION NPs not only delayed disease progression but also prevented melanoma metastasis (Supplementary Fig. 14).

3. Conclusions

Extensive research efforts have been devoted to describe the role of NPs opsonization in systemic delivery, but little attention has been given to its importance *via* lymphatic administration. The interaction of complement proteins with LN resident cells determines the immune pathways elicited upon vaccine administration. Thus, control over the LN trafficking of NPs is vital to regulate the response in the draining LN. Here, we show here the development of a stealth-target balanced approach to achieve efficient activation of medullary APCs in the LN. Our strategy based on zwitterionic-grafted polymeric NPs offers an attractive alternative to the recently questioned PEG for achieving stealth properties. Particles formulated with polysulfobetaine efficiently avoid complement protein adsorption, leading to stealth delivery platforms. Besides, the conjugation of the former NP with the WH targeting peptide to the CLEC9A receptor allows the spatially programmable

release of the mRNA cargo to the medullary APCs, overcoming the architectural barrier of the subcapsular sinus macrophages. With this system, we achieved a strong and antigen-specific humoral and cellular response, while dramatically reducing the pro-inflammatory cascade. Furthermore, the platform shows potential outcome as a prophylactic anti-tumour vaccine, preventing tumour growth and later metastasis.

The ground-breaking approval of mRNA-based nanovaccines is now followed by the demand to expand this immunization approach to a wide range of conditions. However, the inflammatory response elicited by current non-targeted PEG-lipidic formulations hinders their application in autoimmune and autoinflammatory diseases. Here, our proposed zwitterionic-based NPs represent an unprecedented way to balance stealth and targeting properties for safe and controlled release of loaded cargo to the cells of interest. Additionally, zwitterionic polymers exhibit an inherent resistance to protein adsorption and immune recognition, resulting in reduced toxicity and minimal inflammatory responses. This lower toxicity profile of zwitterionic polymers makes them a more attractive option for applications requiring repeated administration or long-term use, further enhancing their potential in diverse biomedical applications.

Surface charge, size, and shape are critical in nanoparticle design for targeted drug delivery and reduced toxicity [55,56]. Surface charge influences interactions with cells and proteins, impacting uptake and biodistribution. Size dictates tissue penetration and cellular uptake efficiency, with smaller particles penetrating tissues more effectively. Nanoparticle shape affects circulation time, uptake mechanisms, and distribution within the body. Optimizing these properties enables precise therapy targeting while minimizing off-target effects and harm. Advances in nanoparticle engineering continuously improve these aspects, enhancing efficacy and safety. Future directions for zwitterionic nanoparticles involve optimizing properties for enhanced targeting and reduced immunogenicity, developing precise delivery strategies, and ensuring scalable manufacturing to improve vaccine effectiveness and advance personalized medicine. Comprehensive testing is crucial to bring these safe, effective innovations into clinical practice, enhancing patient outcomes across various medical fields.

4. Materials and methods

Formulation of polyplexes. Polymer:nucleic acid complexes at different weight ratios were prepared by mixing equal volumes of nucleic acid at 0.5 μg/μL with polymers at different concentrations in sodium acetate buffer solution (12.5 mM, pH 5.5). Optimal OM-pBAE 25:1 weight ratio is shown as an example: 5 μL of mRNA (1 μg/μL) was diluted in 5 μL of sodium acetate buffer to obtain a final concentration of 0.5 μg/μL. 2 μL of OM-pBAE KH (100 μg/μL, 60% lysine modified and 40% histidine modified) was diluted in 98 μL of acetate buffer to obtain a final concentration of 2 μg/μL. Then, nucleic acid was added over polymer solution and mixed by pipetting and incubated at room temperature for 30 min. For OM-pBAE-PEG NPs, 30% of the total pBAE polymer was modified in the lateral hydroxyl chain to include PEG 200 before formulating the particles.

Electrophoretic mobility shift assays (EMSA). To perform mRNA/pDNA retardation assay, different polymer:mRNA/pDNA (*w/w*) ratios were added over agarose gel (2.5% of agarose *w/v*) in Tris-Acetate-EDTA (TAE) buffer containing ethidium bromide (1 μg/mL). Finally, 10 μL of sample was added to the wells and the electrophoresis was performed for 1 h at 80 V (Apelex PS 305, France) and siRNA bands were visualized by UV irradiation.

Transmission Electronic Microscopy (TEM). Sample preparation was performed by placing a 10 μL sample drop on a carbon-coated copper grid. Sample excess was removed by blotting with filter paper. Addition of 10 μL of uranyl acetate (2% w/v) solution was performed for negative staining. The sample was then transferred to the microscope for further visualization. The images were obtained with a JEOL JEM-2001 microscopy (JEOL LTD, Tokio, Japan) operating at 80 kV. Histograms were

performed by counting a population of at least 200 nanoparticles using ImageJ software (Rasband, W·S, ImageJ, U.S. National Institute of Health, Bethesda, Maryland, USA). For protein corona evaluation, nanoparticles were prepared as previously described and incubated in 1:100 FBS dilution in PBS for 2 h at RT. Then, they were directly characterized by TEM microscopy without washing.

Ribogreen assay. Encapsulation efficiency of the nanoparticles was performed using Ribogreen kit for mRNA polyplexes. Nanoparticles were freshly prepared and mixed with Tris-EDTA (TE) buffer and Ribogreen/Picogreen dye. Three standard curves were prepared. First standard curve was a mRNA calibration curve ranging from 0.2 µg/mL to 0.025 µg/mL in TE buffer. Second standard curve was a nucleic acid: nanoparticles calibration with heparin in the same range of concentrations. Heparin is used to disassembly the nanoparticles and deliver the entrapped mRNA, as a competing polyanion. Third and last standard curve was a heparin calibration to remove the background signal. Samples were evaluated both in the presence and absence of heparin and encapsulation efficiency was calculated as follows:

$$EE\% = \left(1 - \left(\frac{free\ mRNA}{total\ mRNA} \right) \right) * 100 \tag{1}$$

Confocal scanning fluorescent microscopy imaging of *in vitro* cell cultures. For CSFM cell imaging, 2×10^5 adherent cells were seeded into each well of a 24-well plate containing a 13-mm gelatin pre-treated glass coverslip. For uptake imaging, Cy3 labelled polyplexes were incubated with the cells for 4 h. Cells were then fixed in 4% (*w/v*) paraformaldehyde, permeabilized with 0.3% Triton X-100 in PBS and blocked in 2% FBS in PBS. Nuclei were stained with DAPI and the coverslips were mounted over slides in Fluoromount-G™ mounting medium. The edge of the cover glass was sealed with nail polish. Images were captured using a confocal laser-scanning fluorescence microscope Leica SP5 (Molecular Probes, Leica Microsystem, Manheim, Germany). For qualitative and quantitative analyses, the ImageJ software with the Fiji plugin was used (Rasband, W·S, ImageJ, U.S. National Institute of Health, Bethesda, Maryland, USA).

Protein corona isolation. A volume of 100 µL of nanoparticles was prepared and incubated in 1 mL of 1:10 fetal bovine sera (FBS) or human sera (HS) dilution in PBS for 2 h at 37 °C. After that, nanoparticles were centrifuged at 15000 rpm for 10 min. A whiteness pellet was observed after centrifugation. The supernatant (SN1) was discarded and the pellet was washed and resuspended in 1 mL of PBS. Second centrifuge was performed, and the supernatant was discarded (SN2). The pellet was resuspended in 10%SDS solution and heated at 95 °C for 10 min in order to denaturalize and separate the proteins that remained attached to nanoparticles (PC).

Total protein quantification by BCA assay. In order to quantify the total amount of protein in the protein corona, a calibration curve of bovine serum albumin (BSA) was prepared by diluting the standard from the kit. Concentrations from 2000 µg/mL to 25 µg/mL were prepared and PBS was used as a negative control. In addition, polyplexes without protein corona were also prepared as a control due to interreferences in the colorimetric test by the oligopeptides present in the polymer. Control values were subtracted to the final measurements. A volume of 200 µL of the working reagent was added to each well in a 96-well plate. Samples were diluted (1:10 and 1:100) in PBS directly from after protein corona isolation. 25 µL aliquots of sample were added to each well. Triplicates were performed for the samples, the controls and the calibration curve. After sample addition, the well plate was covered and incubated at RT for 30 min and the absorbance was measured at 562 nm in a plate reader (Tecan-Infinite 200 Pro) at RT.

Protein corona analysis by SDS-PAGE gels. Sodium dodecyl polyacrylamide (SDS) gels including stacking and running (10% acrylamide) gels were prepared. The stacking portion of the gels is important to retain the polyplexes and free polymer molecules remaining in the protein corona fraction after protein corona isolation. Thus, gels were prepared by polymerizing acrylamide, using ammonium persulfate as imitator and TEMED as accelerator, at the desired percentage. After that, the gels were placed in the plastic electrophoresis chamber and covered with running buffer ($1\times$ SDS-PAGE). Typically, SDS-PAGE analysis was performed after protein quantification analysis by BCA assay. Thus, the required volume of sample from protein corona isolation protocol to charge 30 µg of protein per condition was calculated. Samples were prepared by diluting the calculated volume of protein corona sample in PBS up to 20 µL and 5 µL of loading buffer were added. Gels were run at 120 mV for approximately 2 h and then, stained with Coomassie staining solution (1% Coomassie Brilliant Blue R) in a mixture of water, methanol and glacial acetic acid (9:9:2) for 30 min. After that, gels were incubated in distaining solution (water, methanol and glacial acetic acid (5:4:1). Distaining solution was replaced several times (typically 3) until protein bands became visible. Finally, gels images were analysed by ImageJ software (Rasband, W·S, ImageJ, U.S. National Institute of Health, Bethesda, Maryland, USA) in order to obtain the densitometry profile.

Identification of protein corona by LC/MS. Samples were prepared and charged in the same way as described for SDS-PAGE analysis (2.8.3. Protein corona analysis by SDS-PAGE analysis) but when the protein band started to run in the running gel, the electrophoresis was stopped and stacked band was cut. Peptide fractionation and mass spectrometry were performed at the Vall d'Hebron Institut d'Oncologia facilities, as described previously by Fornaguera et al. (2019). In brief, LC/MS was applied to whole protein fraction analysis using the corresponding protocols to fractionate proteins in peptides. MS/MS fragmentation spectra were obtained by SEQUEST (Bioworks v3.3, ThermoFisher San Jose, CA, USA) using a combined target/decoy database (SwissProt release 15/12), which was constructed reversing protein sequences in the human SwissProt databases. Proteins were identified using MASCOT software. Estimation of relative protein expression to compare the abundance of a certain protein in the protein corona of two different nanoparticles was performed following the method proposed by Vogel et al. [46] We first calculated the total spectral counts N for each sample. This sum includes only peptides of confident identification (above threshold). We then converted them into fractions ($f_i = n_i/N$, where n_i is the total spectral counts for a certain protein and N is the sum of total spectral counts in a sample). We then calculated the overall proportion for each protein as specified in eq. 1. This proportion $f_{i,0}$ is the null expectation in the event that protein i is present at the same level in both samples. This is only accepted for protein which are confidently identified in both samples, and for proteins which are only identified in one sample but assumed to be absent in the other sample. Finally, for each protein a Z-score of differential expression was calculated according to eq. 2.

$$f_{i,0} = \frac{n_{i,1} + n_{i,2}}{n_{i,1} + n_{i,2}} \tag{1}$$

$$Z = \frac{f_{i,1} - f_{i,2}}{\sqrt{\frac{f_{i,0}\left(1 - f_{i,0}\right)}{N_1} + \frac{f_{i,1}\left(1 - f_{i,0}\right)}{N_2}}} \tag{2}$$

where N_1 and N_2 are the total spectral counts in samples 1 and 2, $f_{i,0}$ is the overall proportion of a protein's spectral counts and $f_{i,1}$ and $f_{i,2}$ are the proportions of a protein's spectral counts in sample 1 and 2, respectively.

MTS cell viability evaluation. THP-1 cells were seeded into 96-well plates at a density of 10,000 cells/well. After 24 h, culture medium was replaced with 80 µL fresh supplemented growth medium containing different concentration (1–100 mg of nucleic acid/mL) of nanoparticles. All studies were performed in quintuplicate. 48 h post transfection, 20 µL of manufacturer solution containing MTS/PMS (20:1) was added to each well, and the cells were incubated 3 h. Optical density of each well was measured spectrophotometrically at 490 nm using Tecan (Tecan-Infinite 200 Pro) plate reader. The absorbance values were represented

as the percentage of cell viability taken as 100% cell viability of untreated control cells.

Red Blood Cell (RBC) Lysis Assay. Erythrocytes (RBC, red blood cells) were isolated from fresh whole human blood obtain from healthy donors from the Banc de Sang i Teixits, Barcelona. Blood was diluted with PBS pH 7.4 up to 10 mL and then it was centrifuged (3000 rpm, 10 min, 4 °C) three times, removing the supernatant after each centrifugation and re-suspending the cells in sterile PBS. The final RBC pellet was weighed and re-suspended at 2% (v/v) in PBS. Erythrocytes were counted and diluted to 8×10^9 cells/mL. Aliquots of 10 μL of erythrocytes were added to 100 μL of nanoparticles in a 96-well plate. Two incubation times were evaluated, 10 min and 24 h at 37oC. After incubation, samples were centrifuged at 3000 rpm, for 10 min at 4 °C. The Hb released was assessed by measuring the absorbance at 570 nm using Tecan (Tecan-Infinite 200 Pro) plate reader. The percentage of haemolysis of each sample was calculated relative to 100% haemolysis obtained from incubation with Milli water.

Animals. C57BL/6 mice were obtained from Charles River Mice and bred in-house. Rag2/OT-I (B6.129S7-*Rag1*^{tm1Mom}Tg(TcraTcrb)1100Mjb N9 + N1) mice were kindly provided from Grassi Lab (IRB, Bellinzona). Mice were housed in the specific pathogen-free animal facility of the Institute for Research in Biomedicine (Bellinzona), in individually ventilated cages with controlled light-dark cycle (12:12) and were used between 8 and 12 weeks of age. Animal protocols were approved by the cantonal veterinarian local authorities under the protocol ID: TI33/2021, and the experiments were performed in accordance with the Swiss Federal Veterinary Office guidelines and with the EU Directive 2010/63/EU. Qualitive assessment of the experimental *in vivo* studies was performed following the Animal Research Reportin *In vivo* experiments (ARRIVE).

Bioluminiscence imaging. Mice ($n = 3$) were injected intramuscularly (tibialis anterior muscle) or subcutaneously (footpad) with 50 μg of FLuc complexed with the corresponding polymers. Twenty-four hours after injection, animals were anesthetized and Firefly luciferin was intraperitoneally administered. Thirty minutes later, mice were euthanized, organs of interest collected and *ex vivo* bioluminescence was assessed through radiance measurement. Negative control (non-injected mice) were used to subtract the background signal. Images were treated and analysed using Hokawo v3.0 software.

Popliteal LN collection for imaging. Cy5 labelled polyplexes were administered *via* footpad administration. Six hours after nanoparticle administration, labelled antibodies were injected subcutaneously (except for PB CD21/35, which was injected right after nanoparticle administration in order to obtain a clear signal). One hour after antibody administration, mice were euthanized *via* carbon dioxide and popliteal LNs were collected. They were kept in PBS, in an ice-box for the following steps.

Confocal imaging of *ex vivo* samples. Sample preparation was performed following Virgilio et al. (2022) method. For mouse confocal microscopy experiments, organs were fixed immediately after collection in 4% paraformaldehyde (PFA) for 12 h at 4 °C, then washed in PBS and embedded in 4% Low Gelling Temperature Agarose. 50 μm sections were cut with a vibratome (VT1200S, Leica). Slices were stained in blocking buffer composed of TritonX100 0.1–0.3%, BSA 5% and fluorescently labelled antibodies at appropriate concentration, all diluted in PBS supplemented with calcium and magnesium (PBS+). All antibodies were used at 2 μg/mL and obtained from Biolegend, unless otherwise specified (anti-CD21/35 (CR1/CR2) for follicular dendritic cells, anti-CD169 (Siglec-1) for macrophages and anti-CD11c for dendritic cells). After 48 h of incubation at 4 °C, samples were washed in 0.05% Tween® 20, fixed in PFA 4%, washed in PBS-(without calcium and magnesium) and mounted on glass slides. Confocal images were acquired using Leica TCS SP5 microscope with 20 × 0.7 oil objective. Laser power were kept constant between samples in order to quantify and compare the mean fluorescence signal. LN regions were manually identified based on CD21/35 and CD169 expression. Next, we quantified the total Cy5

polyplex signal in each of the pre-defined regions. Images were treated and analysed using ImageJ software (Rasband, W·S, ImageJ, U.S. National Institute of Health, Bethesda, Maryland, USA).

Two-photon microscopy. Sample preparation was performed following the method of Cordeiro et al. (2019). For mouse two-photon microscopy experiments, nanoparticles and antibodies were previously injected as described in section 4.2.2.1. and, organs were used immediately after collection and mounted on a slide with PBS. All antibodies were used at 2 μg/mL and obtained from Biolegend, unless otherwise specified (anti-CD21/35 (CR1/CR2) for follicular dendritic cells, anti-CD169 (Siglec-1) for macrophages and anti-CD11c for dendritic cells). Images were acquired with LaVision Trimscope II upright two-photon microscope (LaVision Biotec, Bielefeld, Germany) with a 10× (Plan Apo Lambda NA 0.45, Nikon Instruments, NY,USA) dry objective. Excitation was performed with two Chameleon Vision Ti:Sa lasers (Coherent, CA, USA) tuned at 830 and 925 nm, respectively. Images were z-stacks was done, were acquired with a pixel size of 1.07 μm and z-step of 5 μm, for a total imaging depth of around 350 μm. Image analysis was conducted with ImageJ software (Rasband, W·S, ImageJ, U.S. National Institute of Health, Bethesda, Maryland, USA) and 3D reconstruction was performed using Imaris 9.7.2 Cell Imaging Software (Oxford Instruments).

Flow Cytometry. Popliteal LNs were collected, disrupted with tweezers and enzymatically digested for 10 min at 37 °C. DNase I, Dispase and Collagenase P were resuspended in PBS (without calcium and magnesium). Digestion was stopped using a solution of 2 mM EDTA and 2% of FBS diluted in PBS (without calcium and magnesium). We blocked Fc receptors and performed surface staining (anti-CD21/35 (CR1/CR2), anti-CD169, anti-CD11c, anti-B220 (CD45R), anti-Gr-1, anti-NK1.1, anti-CD11b, anti-F4/80 and anti-MCHII). Stained cells were run through LSRFortessa or FACSymphony (BD Biosciences) and data were analysed using FlowJo 10.7.1. software (FlowJo LLC).

Pro-inflammatory cytokines. To measure cytokine and chemokine expression in the serum, LEGENDPlex assays were used according to manufacturer's instructions. Briefly, blood was collected from the cheek (submandibular) (50 μL). The blood was allowed to clot for at least 30 min and centrifuged of 10 min at 1000 x*g*. Serum was collected and assayed immediately. Reagents was prepared following the manufacturer's indications and standards and samples were prepared according to the indicated serial dilutions. The assay was performed in filter plate and samples were transferred to FACS tubes prior to flow cytometry.

CD8$^+$ T cell isolation from the spleen. Spleens from Rag2/OT1 mice were collected, disrupted with tweezers and enzymatically digested for 10 min at 37 °C. DNase I, Dispase and Collagenase D were resuspended in PBS (without calcium and magnesium). Digestion was stopped using a solution of 2 mM EDTA and 2% of FBS diluted in PBS (without calcium and magnesium). Next, incubation with RBC lysis buffer for 5 min in ice was done. Aggregates were removed by passing cell suspension through 70 μm nylon strainer. Cells were centrifuged at 300 x*g* for 10 min and resuspended at 1×108 cell/mL in PBS containing 2% FBS (without calcium and magnesium) and 1 mM EDTA. Once single cell suspension was obtained, manufacturer's recommendations were followed (EasySep™ mouse CD8$^+$ T cell isolation kit). Briefly, rat serum was added to the sample, followed by the isolation cocktail. After 10 min incubation at RT the RapidSpheres™ were added and diluted in 2% FBS diluted in PBS (without calcium and magnesium). Finally, magnetic separation was performed using EasySep™ magnet. Cells were diluted to the required concentration for the following steps using supplemented RPMI-1640.

CFSE staining. Isolated CD8$^+$ T cells were centrifuged and resuspended in PBS at the recommended concentration by the manufacturer (10^6 cells/mL). The appropriated volume of CFSE stock solution was added to the cells and they were incubated for 20 min at RT, protected from light. Next, five times the original staining volume of 2% FBS diluted in PBS (without calcium and magnesium) and incubated for 5 min to remove the unreacted free dye. Finally, cells were pelleted by

centrifugation and resuspended in fresh supplemented RPMI-1640.

Dendritic Cell Isolation from the spleen. Spleens from C57BL/6 mice were collected, disrupted with tweezers and enzymatically digested for 10 min at 37 °C. DNase I, Dispase and Collagenase D were resuspended in PBS (without calcium and magnesium). Digestion was stopped using a solution of 2 mM EDTA and 2% of FBS diluted in PBS (without calcium and magnesium). Next, incubation with RBC lysis buffer for 5 min in ice was done. Aggregates were removed by passing cell suspension through 70 μm nylon strainer. Cells were centrifuged at 300 xg for 10 min and resuspended at 1×108 cell/mL in PBS containing 2% FBS (without calcium and magnesium) and 1 mM EDTA. Once single cell suspension was obtained, manufacturer's recommendations were followed (Pan Dendritic Cell Isolation Kit). Next steps were performed on ice. Cells were counted and resuspended to have 10^8 cells in total. FcR blocking reagent and antibody cocktail were added and incubated for 10 min at 2–8 °C. Cells were washed and centrifuged to finally add the anti-biotin microbeads. After mixing and 10 min incubation at 2–8 °C, we proceeded to magnetic separation using LS columns. Eluted volume represented the enriched dendritic cell fraction.

Dendritic cell: CD8$^+$ T cell co-culture. Dendritic cells were seeded at 5×10^5 cells/well in a round bottom 96-well plate in supplemented RPMI-1640 media. After 1 h of incubation at 37 °C, 2×10^5 CFSE labelled CD8$^+$ T cells were added per well. The co-culture was pulsed with the OVA mRNA nanoparticles for 4 h. OVA protein (10 μg/well) was added as positive control and GFP mRNA nanoparticles as negative control. Then, cells were centrifuged and fresh media added. Cells were co-cultured for 3 days and daily check by microscopy to assess T cell proliferation. After 3 days, immunostaining was performed. CD8$^+$ T cells were labelled using anti-CD3 antibody (clone 17A2) and flow cytometry was done.

Enzyme-Linked ImmunoSorbent (ELISA) Assay. Briefly, blood was collected from the cheek (submandibular) (50 μL) on days 7, 14 and 21 post-injection and directly used. The blood was allowed to clot for at least 30 min and centrifuged of 10 min at 1000 xg. Serum was collected and assayed immediately. A day prior conducting the experiment, 96-well flat-bottom plate Nunc™ were coated by adding 25 μL of OVA protein solution (1 mg/mL) and incubated overnight at 4 °C. The next day, the antigen was removed and the wells were blocked by adding 50 μL of 1% BSA PBS solution. The blocking buffer was incubated for 1 h at RT. Next, we washed the plate three times using PBS-Tween solution and one extra time with PBS. In parallel, we prepared the serial dilutions of serum (in the range of 1/10 to 1/10000) in 1% BSA PBS solution, in a new 96-well plate. Then, we transferred the serum dilutions to the OVA coated ELISA Nunc™ 96-well plate and incubate them for 1 h at RT. After the incubation, we repeat the washing steps and we finally added the primary antibody conjugated to alkaline phosphatase (1:500 in 1% BSA PBS solution). Next, we incubate the alkaline phosphatase conjugate antibody (goat anti-mouse IgM or IgG from Southern Biotech; Birminghan (AL), USA) for 1 h at RT and we washed the plate again. Finally, we added the alkaline phosphatase substrate and incubate it for 30 min, to avoid saturation. The reaction was stopped by adding NaOH 3 M and the well plate was read at 405 nm.

Immunization and tumour therapy experiments. Six- to eight-week-old mice ($n = 10$ for each group) were immunized by subcutaneous injection into the footpad of OVA mRNA WH-ZION NPs (25 μg/mouse) or OVA protein (25 μg/mouse) in a maximum volume of 10 μL. After six days, animals were injected subcutaneously with B16F1/OVA melanoma cells (1×105) into the footpad of mice. Tumour growth was subsequently measured twice or three times a week using a digital caliper and calculated as 0.5 x length x width2 by blinded investigators. Mice were killed when the tumour volumes reached 800 mm3.

Statistical analysis. For immunogenicity measurements and tumour therapy experiments, we used groups of three to ten animals per group. Statistical analysis was performed using Microsoft Excel and Prism 8.0 (GraphPad). Data are expressed as means ± s.e.m. Data were analysed by Student's t-test. All t-tests were one-tailed and unpaired and were considered statistically significant if $P < 0.05$ (*$P < 0.05$, $P < 0.01$, *$P < 0.001$, unless otherwise indicated).

CRediT authorship contribution statement

Coral García-Fernández: Writing – original draft, Software, Methodology, Investigation. **Tommaso Virgilio:** Writing – review & editing, Methodology, Investigation. **Irene Latino:** Writing – review & editing, Methodology, Investigation. **Marta Guerra-Rebollo:** Writing – review & editing, Software, Methodology. **Santiago F. Gonzalez:** Writing – review & editing, Funding acquisition, Formal analysis, Data curation, Conceptualization. **Salvador Borrós:** Writing – review & editing, Visualization, Validation, Supervision, Funding acquisition, Conceptualization. **Cristina Fornaguera:** Writing – review & editing, Validation, Supervision, Resources, Project administration, Funding acquisition, Formal analysis, Conceptualization.

Data availability

Data will be made available on request.

Acknowledgements

Appendix A. Supplementary data

Supplementary data to this article can be found online at https://doi.org/10.1016/j.jconrel.2024.08.018.

References

[1] X. Tian, S. Angioletti-Uberti, G. Battaglia, Sci. Adv. 6 (2020) 1.
[2] A.J. McGoron, Bioconjug. Chem. 31 (2020) 436.
[3] B.B. Mendes, J. Conniot, A. Avital, D. Yao, X. Jiang, X. Zhou, N. Sharf-Pauker, Y. Xiao, O. Adir, H. Liang, J. Shi, A. Schroeder, J. Conde, Nat. Rev. Methods Prim. 21 (2022), 2(24).
[4] M.S. Gebre, S. Rauch, N. Roth, J. Gergen, J. Yu, X. Liu, A.C. Cole, S.O. Mueller, B. Petsch, D.H. Barouch, npj Vaccines 71 (2022), 7(1).
[5] E. Rohner, R. Yang, K.S. Foo, A. Goedel, K.R. Chien, 40, 1586, Nat. Biotechnol. 4011 (2022) 2022.
[6] M.F. Bachmann, G.T. Jennings, 10, 787, Nat. Rev. Immunol. 1011 (2010) 2010.
[7] L. Miao, Y. Zhang, L. Huang, Mol. Cancer 201 (2021), 20(1).
[8] M.J. Lin, J. Svensson-Arvelund, G.S. Lubitz, A. Marabelle, I. Melero, B.D. Brown, J. D. Brody, 3, 911, Nat. Can. 38 (2022) 2022.
[9] J.E. Chang, S.J. Turley, Trends Immunol. 36 (2015) 30.
[10] S.M. Grant, M. Lou, L. Yao, R.N. Germain, A.J. Radtke, J. Cell Sci. 133 (2020) 133.
[11] J. Crecente-Campo, T. Virgilio, D. Morone, C. Calviño-Sampedro, I. Fernández-Mariño, A. Olivera, R. Varela-Calvino, S.F. González, M.J. Alonso, Nanomedicine 14 (2019) 3013.
[12] Y.-N. Zhang, J. Lazarovits, W. Poon, B. Ouyang, N.M. Nguyen Luan, B.R. Kingston, W.C.W. Chan, P. Program, Nano Lett. 19 (2019) 7226.
[13] T.G. Phan, I. Grigorova, T. Okada, J.G. Cyster, Nat. Immunol. 8 (2007) 992.
[14] S.T. Reddy, A.J. Van Der Vlies, E. Simeoni, V. Angeli, G.J. Randolph, C.P. O'Neil, L. K. Lee, M.A. Swartz, J.A. Hubbell, Nat. Biotechnol. 25 (2007) 1159.
[15] R. Tavano, L. Gabrielli, E. Lubian, C. Fedeli, S. Visentin, P. Polverino De Laureto, G. Arrigoni, A. Geffner-Smith, F. Chen, D. Simberg, G. Morgese, E.M. Benetti, L. Wu, S.M. Moghimi, F. Mancin, E. Papini, ACS Nano 12 (2018) 5834.
[16] M. Barani, M. Mirzaei, M. Torkzadeh-Mahani, A. Lohrasbi-Nejad, M. H. Nematollahi, Mater. Sci. Eng. C 113 (2020) 110975.
[17] M.J. Mitchell, M.M. Billingsley, R.M. Haley, M.E. Wechsler, N.A. Peppas, R. Langer, 20, 101, Nat. Rev. Drug Discov. 202 (2020) 2020.
[18] P. Sellaturay, S. Nasser, S. Islam, P. Gurugama, P.W. Ewan, Clin. Exp. Allergy 51 (2021) 861.
[19] M.D. McSweeney, M. Mohan, S.P. Commins, S.K. Lai, Front. Allergy 2 (2021) 1.
[20] B.M. Chen, T.L. Cheng, S.R. Roffler, ACS Nano 15 (2021) 14022.

[21] Q. Yang, T.M. Jacobs, J.D. McCallen, D.T. Moore, J.T. Huckaby, J.N. Edelstein, S. K. Lai, ACS Publ. 88 (2016) 11804.
[22] B.M. Chen, Y.C. Su, C.J. Chang, P.A. Burnouf, K.H. Chuang, C.H. Chen, T.L. Cheng, Y.T. Chen, J.Y. Wu, S.R. Roffler, Anal. Chem. 88 (2016) 10661.
[23] S. Zalba, T.L.M. ten Hagen, C. Burgui, M.J. Garrido, J. Control. Release 351 (2022) 22.
[24] M. Ibrahim, T. Shimizu, H. Ando, Y. Ishima, O.H. Elgarhy, H.A. Sarhan, A. K. Hussein, T. Ishida, J. Control. Release 354 (2023) 260.
[25] Y. Ju, W.S. Lee, E.H. Pilkington, H.G. Kelly, S. Li, K.J. Selva, K.M. Wragg, K. Subbarao, T.H.O. Nguyen, L.C. Rowntree, L.F. Allen, K. Bond, D.A. Williamson, N.P. Truong, M. Plebanski, K. Kedzierska, S. Mahanty, A.W. Chung, F. Caruso, A. K. Wheatley, J.A. Juno, S.J. Kent, ACS Nano 16 (2022) 11769.
[26] S.M. Moghimi, D. Simberg, Mol. Ther. 30 (2022) 2109.
[27] N. Segovia, P. Dosta, A. Cascante, V. Ramos, S. Borrós, Acta Biomater. 10 (2014) 2147.
[28] Z.G. Estephan, P.S. Schlenoff, J.B. Schlenoff, Langmuir 27 (2011) 6794.
[29] C.A. Del Grosso, C. Leng, K. Zhang, H.C. Hung, S. Jiang, Z. Chen, J.J. Wilker, Chem. Sci. 11 (2020) 10367.
[30] H. Qian, K. Wang, M. Lv, C. Zhao, H. Wang, S. Wen, D. Huang, W. Chen, Y. Zhong, J. Control. Release 343 (2022) 492.
[31] Q. Shao, Y. He, A.D. White, S. Jiang, J. Chem. Phys. 136 (2012) 225101.
[32] P. Dosta, V. Ramos, S. Borrós, Mol. Syst. Des. Eng. 3 (2018) 677.
[33] C. Fornaguera, M. Guerra-Rebollo, M. Ángel Lázaro, C. Castells-sala, O. Meca-Cortés, V. Ramos-pérez, A. Cascante, N. Rubio, J. Blanco, S. Borrós, M.Á. Lázaro, C. Castells-sala, O. Meca-Cortés, V. Ramos-pérez, A. Cascante, N. Rubio, J. Blanco, S. Borrós, M. Ángel Lázaro, C. Castells-sala, O. Meca-Cortés, V. Ramos-pérez, A. Cascante, N. Rubio, J. Blanco, S. Borrós, Adv. Healthc. Mater. 7 (2018) 1800335.
[34] P. Cabanach, A. Pena-Francesch, D. Sheehan, U. Bozuyuk, O. Yasa, S. Borros, M. Sitti, Adv. Mater. 32 (2020) 2003013.
[35] R. Texidó, P. Cabanach, R. Kaplan, C. García-Bonillo, D. Pérez, S. Zhang, S. Borrós, A. Pena-Francesch, R. Texidó, P. Cabanach, C. García-Bonillo, D. Pérez, S. Borrós, R. Kaplan, S. Zhang, A. Pena-Francesch, Adv. Mater. Interfaces 9 (2022) 2201152.
[36] Z. Yan, Y. Wu, J. Du, G. Li, S. Wang, W. Cao, X. Zhou, C. Wu, D. Zhang, X. Jing, Y. Li, H. Wang, Y. Gao, Y. Qi, Oncotarget 7 (2016) 40437.
[37] F.F. Gu, K. Zhang, L.L. Ma, Y.Y. Liu, C. Li, Y. Hu, Q.F. Yang, J.Y. Liang, Y.L. Zeng, Y. Wang, L. Liu, Front. Immunol. 11 (2020) 1513.
[38] J. Grabowska, M.A. Lopez-Venegas, A.J. Affandi, J.M.M.M. Den Haan, Front. Immunol. 9 (2018) 2472.
[39] S.M. Moghimi, D. Simberg, Mol. Ther. 30 (2022) 2109.
[40] R. Cosialls, O. Fernández, C. Simó, K.R. Pulagam, M. Guerra-Rebollo, J. Llop, C. Fornaguera, A.B. Cuenca, S. Borrós, J. Control. Release 358 (2023) 739.
[41] M. Navalón-López, A. Dols-Perez, S. Grijalvo, C. Fornaguera, S. Borrós, Nanoscale Adv. 5 (2023) 1611.
[42] T. Granot, T. Senda, D.J. Carpenter, T. Connors, B. Reizis, Immunity 46 (2017) 504.
[43] F.J. Cueto, C. del Fresno, D. Sancho, Front. Immunol. 10 (2020) 3146.
[44] L. Woythe, P. Madhikar, N. Feiner-Gracia, C. Storm, L. Albertazzi, ACS Nano 16 (2022) 3785.
[45] S.M. Moghimi, D. Simberg, E. Papini, Z.S. Farhangrazi, Adv. Drug Deliv. Rev. 157 (2020) 83.
[46] C. Vogel, E.M. Marcotte, 3, 1444, Nat. Protoc. 39 (2008) 2008.
[47] P. Brugada-Vilà, A. Cascante, M.Á. Lázaro, C. Castells-Sala, C. Fornaguera, M. Rovira-Rigau, L. Albertazzi, S. Borros, C. Fillat, Theranostics 10 (2020) 2744.
[48] S.F. Gonzalez, V. Lukacs-Kornek, M.P. Kuligowski, L.A. Pitcher, S.E. Degn, S. J. Turley, M.C. Carroll, J. Immunol. 185 (2010) 2659.
[49] S.F. Gonzalez, V. Lukacs-Kornek, M.P. Kuligowski, L.A. Pitcher, S.E. Degn, Y. A. Kim, M.J. Cloninger, L. Martinez-Pomares, S. Gordon, S.J. Turley, M.C. Carroll, Nat. Immunol. 11 (2010) 427.
[50] S.F. Gonzalez, S.E. Degn, L.A. Pitcher, M. Woodruff, B.A. Heesters, M.C. Carroll, Annu. Rev. Immunol. 29 (2011) 215.
[51] A. Bergtold, D.D. Desai, A. Gavhane, R. Clynes, Immunity 23 (2005) 503.
[52] S. Tahtinen, A.J. Tong, P. Himmels, J. Oh, A. Paler-Martinez, L. Kim, S. Wichner, Y. Oei, M.J. McCarron, E.C. Freund, Z.A. Amir, C.C. de la Cruz, B. Haley, C. Blanchette, J.M. Schartner, W. Ye, M. Yadav, U. Sahin, L. Delamarre, I. Mellman, 23, 532, Nat. Immunol. 234 (2022) 2022.
[53] T. Velikova, T. Georgiev, Rheumatol. Int. 41 (2021) 509.
[54] J.R. Teijaro, D.L. Farber, 21, 195, Nat. Rev. Immunol. 214 (2021) 2021.
[55] X. He, Z. Jiang, O.U. Akakuru, J. Li, A. Wu, Chem. Commun. 57 (2021) 12417.
[56] Y. Luo, J. Zhao, X. Zhang, C. Wang, T. Wang, M. Jiang, Q. Zhu, T. Xie, D. Chen, Colloids Surf. B: Biointerfaces 201 (2021) 111638.